



## Research Paper

# Role of oxygen vacancies in photocatalytic water oxidation on ceria oxide: Experiment and DFT studies



Yong-Chao Zhang<sup>a,b</sup>, Zheng Li<sup>a,b</sup>, Lei Zhang<sup>a,b</sup>, Lun Pan<sup>a,b</sup>, Xiangwen Zhang<sup>a,b</sup>, Li Wang<sup>a,b</sup>, Fazal-e-Aleem<sup>c</sup>, Ji-Jun Zou<sup>a,b,\*</sup>

<sup>a</sup> Key Laboratory for Green Chemical Technology of Ministry of Education, School of Chemical Engineering and Technology, Tianjin University, China

<sup>b</sup> Collaborative Innovative Center of Chemical Science and Engineering (Tianjin), Tianjin 300072, China

<sup>c</sup> Department of Physics, The University of Lahore, 1-Km, Raiwind Road, Lahore, 54600, Pakistan

## ARTICLE INFO

**Keywords:**  
Photocatalysis  
Water oxidation  
Water splitting  
 $\text{CeO}_2$   
Oxygen vacancy  
DFT computation

## ABSTRACT

Photocatalytic water oxidation suffers from sluggish kinetics and remains the bottleneck for water splitting. Here, using  $\text{CeO}_2$  nanorods as model photocatalyst we studied the critical role of oxygen vacancies in photocatalytic water oxidation. First  $\text{CeO}_2$  nanorods with similar morphology but different concentration of oxygen vacancies were fabricated by one-step hydrothermal method with in-situ reducing treatment. The optical absorption, charge transfer efficiency, and photocatalytic activity in oxygen generation were found closely dependent on the concentration of oxygen vacancies. Then density functional theory calculations were conducted to unveil the role of oxygen vacancies and understand the water oxidation mechanism. It was found the presence of oxygen vacancies narrows the bandgap and modulates the electronic structure for accelerating the charge transfer, in good agreement with the experimental observations. The overall oxygen generation pathway was screened and the oxygen vacancies were found to lower the barrier energy for the rate limiting step of O–O bond formation and restrain the reverse reaction of O and H, thus the  $\text{O}_2$  generation kinetics on oxygen-defective  $\text{CeO}_2$  are improved significantly. This study provides in-depth understanding on the critical role of oxygen vacancies in photocatalytic water oxidation and is helpful for designing highly efficient photocatalyst to overcome the bottleneck of water splitting.

## 1. Introduction

Photocatalytic water splitting is an effective way to harvest and utilize solar energy and produce hydrogen energy [1–5]. This process involves two reactions, namely hydrogen evolution and oxygen evolution. The first one has achieved much improvement in recent years [6], but oxygen evolution with a complex four electrons water oxidation remains a bottleneck to limit the efficiency due to the very slow kinetics [7–10]. Exploring a catalyst with high reactivity and capability of harvesting visible light is crucial and essential for photocatalytic water oxidation, though it remains a great challenge. Ceria ( $\text{CeO}_2$ ) has been regarded as an attractive photocatalyst for oxygen evolution due to its strong redox capacity [11]. For example, Au/ $\text{CeO}_2$  is reported to show high activity for visible-light-driven oxygen generation by means of surface-plasmon resonance effect [12], and  $\text{CeO}_2$  nanorods with stepped (110) and (100) planes are much more active as compared with  $\text{CeO}_2$  nanoparticles mainly exposed with (111) facets [13–16].

However, the wide band gap of  $\text{CeO}_2$  (3.2 eV) depresses the ability

of harvesting visible light [11]. Oxygen vacancies (Vo) in metal oxides bring many benefits for photocatalysis like creating visible light adsorption by generating isolated level below the conduction band and improving the donor density and electrical conductivity by providing shallow donors [17–22]. Actually, it has been reported that  $\text{CeO}_2$  with oxygen vacancies exhibits good visible-light activity in photo-degradation of organic pollutants [23].

Furthermore, the detailed mechanism of water oxidation is complicated and not fully understood, especially the formation of O–O bond [24–26]. Therefore, unraveling the complex mechanism of water oxidation and the dependence of performance on structure are important for designing highly efficient photocatalyst. In this work, we choose  $\text{CeO}_2$  as model to study the role of oxygen vacancies on photocatalytic water oxidation. Experimental study shows the oxygen-defective  $\text{CeO}_2$  nanorods exhibit enhanced visible-light-harvesting, low electro-hole recombination and high oxygen evolution activity. Density functional theory (DFT) calculation confirms the presence of oxygen vacancies on  $\text{CeO}_2$ (110) effectively narrows the band gap, modulates

\* Corresponding author at: Key Laboratory for Green Chemical Technology of Ministry of Education, School of Chemical Engineering and Technology, Tianjin University, China.  
E-mail address: [jj\\_zou@tju.edu.cn](mailto:jj_zou@tju.edu.cn) (J.-J. Zou).

the electronic structure to accelerate the charge transfer, and benefits the  $\text{H}_2\text{O}$  dehydrogenation and  $\text{O}_2$  formation. So this work unveils the critical role of oxygen vacancies on photocatalytic oxygen generation, which is helpful for designing highly efficient photocatalyst to overcome the bottleneck of water splitting.

## 2. Experiments and methods

### 2.1. Synthesis of $\text{CeO}_2$ nanorods with and without oxygen vacancies

All the chemicals were purchased and used without further purification.  $\text{CeO}_2$  nanorods with oxygen vacancies were synthesized by modifying previous method [27]. Briefly, in a 100 mL Teflon-lined autoclave  $\text{Ce}(\text{NO}_3)_3 \cdot 6\text{H}_2\text{O}$  (1.736 g) and  $\text{NaOH}$  (19.2 g) were dissolved in distilled water (80 mL), afterward a certain amount (0.12, 0.24 and 0.48 g) of  $\text{NaBH}_4$  was added and the solution was sealed and heated at 100 °C for 24 h. In this process,  $\text{NaBH}_4$  serves as the reducing agent to in-situ generate oxygen vacancies during the growth of nanorods, and the concentration of oxygen vacancies can be controlled by the amount of  $\text{NaBH}_4$  added. After cooling to room temperature, the precipitates were collected and then dispersed in a 1.0 M hydrochloric acid solution with stirring for 15 h at room temperature to remove  $\text{NaBO}_2$  byproduct and residual  $\text{NaBH}_4$ . The resultant powders were collected through centrifugation, washing, and then drying at 60 °C overnight under vacuum. The final samples were labeled as  $\text{CeO}_2$ -NRs-1,  $\text{CeO}_2$ -NRs-2 and  $\text{CeO}_2$ -NRs-3, according to the amount of  $\text{NaBH}_4$  added (0.12, 0.24 and 0.48 g), respectively. As reference, pristine  $\text{CeO}_2$  nanorods ( $\text{CeO}_2$ -NRs) were prepared by hydrothermal method without  $\text{NaBH}_4$ .

### 2.2. Characterizations of catalysts

X-ray diffraction (XRD) patterns were recorded on D/MAX-2500 X-ray diffractometer equipped with  $\text{Cu K}\alpha$  radiation with a scanning rate of 5°/min. Transmission electron microscope (TEM) and high resolution transmission electron microscope (HRTEM) observations were carried out on a Tecnai G2 F20 transmission electron microscope with an acceleration voltage of 200 kV. X-ray photoelectron spectroscopy (XPS) analysis was conducted with thermos ESCALAB 250XI system using  $\text{Al K}\alpha$  radiation, and C 1 s peak (284.8 eV) of contamination carbon was applied to calibrate binding energy. Raman spectra patterns were measured by an inVia reflex DXR Microscope. Electron paramagnetic resonance (EPR) spectra were obtained by Bruker E500 spectrometer at 25 °C. Brunauer-Emmett-Teller specific surface area was calculated according to the nitrogen adsorption/desorption isotherms measured at –196 °C on a Micromeritics TriStar 3000 instrument. Photo-luminescence (PL) spectra were measured by a Horiba JobinYvon Fluorolog3-21 under the excitation light of 325 nm, and the UV-vis spectra were measured on Hitachi U-3010 spectrometer. Electrochemical impedance spectroscopy (EIS) measurements were carried out with a sinusoidal ac perturbation of 10 mV applied over the frequency range of 0.01–10<sup>5</sup> Hz.

### 2.3. Photocatalytic oxygen evolution

The photocatalytic oxygen generation reaction was conducted in a 120 mL closed reactor. 50 mg photocatalyst was dispersed in 100 mL distilled water with 0.17 g  $\text{AgNO}_3$  as the electron sacrificial agent. After ultrasonic treatment 30 min, the reaction system was purged with argon gas to remove the dissolved air. Then, 300 W Xe lamp (PLS-SXE 300/300UV, Beijing Perfectlight Technology Co. Ltd.) with a UV cutoff filter ( $\lambda > 420$  nm) vertically irradiated the reaction system from the upside position, the light density was 43 mW/cm<sup>2</sup> at 420 nm. The temperature was maintained at 0 °C, and the total reaction time was 4 h. The gas containing  $\text{O}_2$  and Ar was withdrawn and analyzed by using Bruker 450-GC gas chromatograph equipped with a 5 Å molecular sieve column and thermal conductivity detector, argon (99.999%) as

carrier gas.

### 2.4. Computational details

All DFT calculations were performed by using the Vienna ab initio simulation package (VASP) [28,29]. The generalized gradient approximation (GGA) with Perdew-Burker-Ernzerhof (PBE) functional was applied to address the nonlocal exchange correlation energy [30]. To eliminate the error from strong self-interaction of localized Ce 4f-orbital, DFT + U method with the  $U_{\text{eff}} = 5.0$  eV was used in all calculations [31,32]. The kinetic cutoff energy of 400 eV was adopted, and the Brillouin zone integration was sampled with the  $3 \times 3 \times 1$  k-point mesh. Structure optimization was deemed as converged until the force of all atoms less than 0.05 eV/Å, and the criteria of energy convergence was set to  $1 \times 10^{-5}$  eV. For the whole water oxidation reaction process, the climbing image nudged elastic band (Cl-NEB) method was performed to locate the corresponding transition states (TS) [33].

Before model construction,  $\text{CeO}_2$  bulk cell was optimized with a  $6 \times 6 \times 6$  k-point grid. The optimized lattice parameter is 5.473 Å, in agreement with the experimental value of 5.411 Å [34].  $\text{CeO}_2$ (110) was used because the real  $\text{CeO}_2$  nanorods exposed mainly with (110) facet according to the experiment results. As shown in Fig. 1a and b, a p ( $2 \times 2$ ) periodically repeated slab with five layers was constructed to represent the model of perfect  $\text{CeO}_2$ (110). During optimization, the bottom two layers were fixed in their bulk position, and others were fully relaxed. The vacuum region was set to 15 Å to avoid two slabs interaction. The model of  $\text{CeO}_2$ (110) is enough and suitable for our calculation after verification (Table S1). Similar to the previous calculation [35,36] and our experiment results (see below), one sub-surface oxygen atom from the perfect  $\text{CeO}_2$ (110) was removed to simulate the oxygen defective  $\text{CeO}_2$ (110) with a formation energy of 268.1 kJ/mol (Fig. 1c and d). The adsorption energy ( $E_{\text{ads}}$ ) is defined as follows.

$$E_{\text{ads}} = E_{\text{adsorbate/surface}} - E_{\text{adsorbate}} - E_{\text{substrate}}$$

where  $E_{\text{adsorbate/surface}}$ ,  $E_{\text{adsorbate}}$  and  $E_{\text{substrate}}$  represent the energies of substrate with the adsorbate species, the adsorbate molecule, and the substrate, respectively. A negative value means the process is exothermic adsorption.

## 3. Results and discussion

### 3.1. Structure characteristic of catalysts

Oxygen-defective  $\text{CeO}_2$  nanorods were synthesized via one-step hydrothermal method with in-situ reducing treatment. Fig. 2a shows the typical XRD pattern of as-prepared  $\text{CeO}_2$  nanorods, from which eight main diffraction peaks at  $2\theta = 28.54^\circ$ ,  $33.04^\circ$ ,  $47.43^\circ$ ,  $56.31^\circ$ ,  $59.08^\circ$ ,  $69.33^\circ$ ,  $76.68^\circ$  and  $79.05^\circ$  belonging to the (111), (200), (220), (311), (222), (400), (331) and (420) plane of cubic fluorite ceria (JCPDS card: 34-0394) are observed. There is no phase change in oxygen-defective  $\text{CeO}_2$  compared with the pristine one, and no peak of any other impurity is detected. TEM images in Fig. 2b–e show that  $\text{CeO}_2$  exhibits nanorods morphology with the length of pristine  $\text{CeO}_2$ -NRs as about 95 nm and the diameter as about 9.0 nm. The adding of reductant in the synthesis makes the rods slightly shorter and bigger, but does not change the overall morphology. HRTEM image and electron diffraction in Fig. 2f further reveals the nanorods are polycrystalline faceted with mainly (110). The specific surface area changes slightly in range of 98–112 m<sup>2</sup> g<sup>-1</sup> (Table 1).

To reveal oxygen vacancies of  $\text{CeO}_2$  nanorods, EPR, XPS and Raman characterizations were conducted. As shown in Fig. 3a, similar to other metal oxides,  $\text{CeO}_2$  shows a symmetrical EPR signal ( $g = 2.003$ ) originated from the unpaired electrons at oxygen vacancy sites [18,21,37]. Notably,  $\text{CeO}_2$ -NRs-2 shows the strongest signal, followed by  $\text{CeO}_2$ -NRs-1,  $\text{CeO}_2$ -NRs-3 and finally  $\text{CeO}_2$ -NRs, indicating the order of  $\text{V}_o$  concentration in the samples. In particular, the very intensive signal of

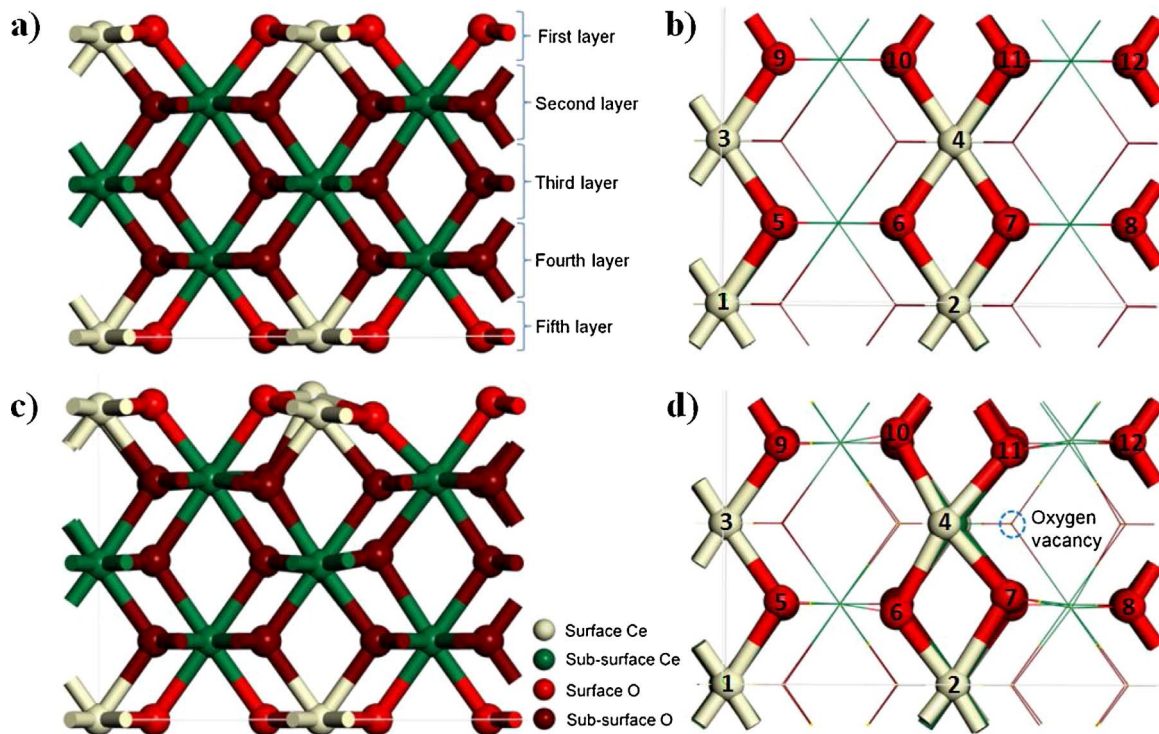


Fig. 1. Optimized surface configuration of  $\text{CeO}_2(110)$ : (a) and (b) are side and top views of perfect  $\text{CeO}_2(110)$ , (c) and (d) are side and top views of oxygen-defective  $\text{CeO}_2(110)$ .

$\text{CeO}_2$ -NRs-2 suggests it is more abundant with Vo compared with  $\text{CeO}_2$ -NRs-1, attributed to the more  $\text{NaBH}_4$  in the synthesis mixture. However the Vo becomes less in  $\text{CeO}_2$ -NRs-3 when more  $\text{NaBH}_4$  are added, probably because large amount of  $\text{NaBO}_2$  are formed on  $\text{CeO}_2$  surface that suppresses the further reduction reaction. In Ce-3d XPS spectra shown in Fig. 3b, the Ce 3d peak of  $\text{CeO}_2$ -NRs-1, 2, and 3 shifts to lower binding energy compared with  $\text{CeO}_2$ -NRs, confirming the formation of oxygen defects on the surface. The peak is further fitted into eight peaks to distinguish  $\text{Ce}^{3+}$  and  $\text{Ce}^{4+}$  species [14,23,27], and Table 1 shows the weight of  $\text{Ce}^{3+}$  based on the integrated area of these peaks increases firstly from  $\text{CeO}_2$ -NRs to  $\text{CeO}_2$ -NRs-1 and  $\text{CeO}_2$ -NRs-2 and then decreases for  $\text{CeO}_2$ -NRs-3, agreeing well with the tendency obtained from EPR measurement in Fig. 3a. Raman spectra in Fig. 3c shows strong signal at  $\sim 450$  and weak peak at  $\sim 600 \text{ cm}^{-1}$  originated from the fluorite type structure vibration [27,38] and the presence of  $\text{Ce}^{3+}$  correlated to oxygen vacancies [27,39], respectively. And the reduced samples show almost four times higher ratio of the two peaks area ( $A_{600}/A_{450}$ ) compared with the pristine counterpart as summarized in Table 1, also confirming the existence of large amount of oxygen vacancies. It is worth noting that, EPR and Raman characterizations show significant difference between the reduced and pristine  $\text{CeO}_2$ , but the difference derived from XPS analysis is relatively small. This suggests that the oxygen vacancies are richer in the inner lattice of  $\text{CeO}_2$ , note XPS can only test the surface layers but EPR and Raman reflect the average structure of the bulk.

### 3.2. Photocatalytic performance of catalysts

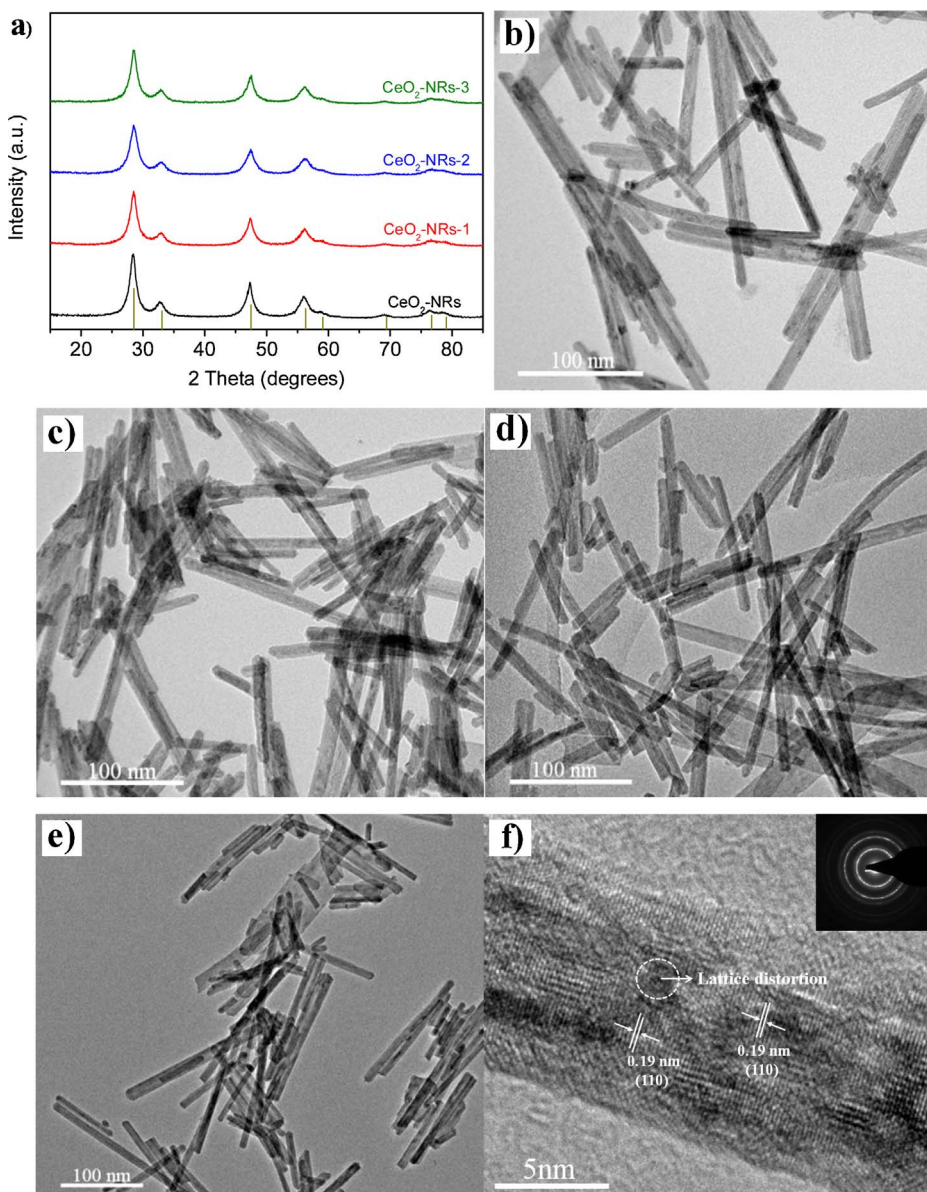
To evaluate the optical properties of  $\text{CeO}_2$  nanorods, UV-vis diffuse reflectance spectroscopy (DRS) was measured, and Fig. 4a shows that the oxygen-defective  $\text{CeO}_2$  samples exhibit extended visible-light adsorption. Specially, the band gap of  $\text{CeO}_2$ -NRs-2 decreased by 0.23 eV compared to  $\text{CeO}_2$ -NRs (2.76 eV), also the band gap of  $\text{CeO}_2$ -NRs-1 and  $\text{CeO}_2$ -NRs-3 are reduced to 2.65 and 2.71 eV respectively. The increased visible light adsorption can be originated from the electron transition from the valence band to oxygen defect level or from the defect level to conduction band [18]. Additionally, the PL spectra in

Fig. 4b demonstrate the oxygen-defective  $\text{CeO}_2$  nanorods have lower PL intensity compared to the pristine sample, and the order of separation efficiency is  $\text{CeO}_2$ -NRs-2 >  $\text{CeO}_2$ -NRs-1 >  $\text{CeO}_2$ -NRs-3 >  $\text{CeO}_2$ -NRs, indicating good dependence on the Vo concentration. The electrochemical impedance spectroscopy (EIS) in Fig. 4c shows that  $\text{CeO}_2$ -NRs-2 has a much smaller arc radius compared to pristine  $\text{CeO}_2$ -NRs, suggesting the very low resistance and fast interfacial charge carrier transfer [40–43].

The photocatalytic oxygen generation was tested under visible light (Fig. 4d). Obviously,  $\text{CeO}_2$ -NRs-2 shows the highest photocatalytic activity with the highest oxygen evolution rate ( $137.7 \text{ umol g}^{-1} \text{ h}^{-1}$ ), followed by the  $\text{CeO}_2$ -NRs-1 ( $101.9 \text{ umol g}^{-1} \text{ h}^{-1}$ ),  $\text{CeO}_2$ -NRs-3 ( $83.5 \text{ umol g}^{-1} \text{ h}^{-1}$ ) and  $\text{CeO}_2$ -NRs ( $78.9 \text{ umol g}^{-1} \text{ h}^{-1}$ ). To eliminate the effect of surface area, the reaction rate was normalized by the surface area. However, these catalysts still show the same tendency of  $\text{CeO}_2$ -NRs-2 ( $1.224 \text{ umol m}^{-2} \text{ h}^{-1}$ ) >  $\text{CeO}_2$ -NRs-1 ( $0.994 \text{ umol m}^{-2} \text{ h}^{-1}$ ) >  $\text{CeO}_2$ -NRs-3 ( $0.887 \text{ umol m}^{-2} \text{ h}^{-1}$ ) >  $\text{CeO}_2$ -NRs ( $0.804 \text{ umol m}^{-2} \text{ h}^{-1}$ ). So it is concluded that the oxygen evolution activity is closely dependent on the concentration of oxygen vacancy in  $\text{CeO}_2$ , namely the more concentration of Vo in  $\text{CeO}_2$ , the higher the oxygen evolution activity.

### 3.3. Influence of oxygen vacancies on electronic structure of $\text{CeO}_2$

In order to get insights on the role of oxygen vacancies, and to understand the reaction mechanism of oxygen evolution, DFT + U calculations were conducted. It is well known that the photo-induced electron/hole strongly depends on the band structure and electronic density of states (DOS) of photocatalyst [44]. As shown in Fig. 5a and b, the valence band (VB) of  $\text{CeO}_2(110)$  is mainly contributed by the O-2p orbit below Fermi level and the conduction band (CB) is ascribed to the Ce-4f orbit above Fermi level. However, the bandgap ( $E_g$ ) is underestimated by using DFT calculation due to the derivative discontinuity of exchange correlation function [45,46]. The presence of oxygen vacancies effectively reduces the bandgap, which is consistent with the enhanced optical absorption in Fig. 4a. The VB width of oxygen-defective  $\text{CeO}_2(110)$  increases compared to that of perfect  $\text{CeO}_2(110)$ , predicting a higher holes mobility and a better photocatalytic oxidation



**Fig. 2.** (a) XRD patterns, TEM images of (b) CeO<sub>2</sub>-NRs, (c) CeO<sub>2</sub>-NRs-1, (d) CeO<sub>2</sub>-NRs-2, (e) CeO<sub>2</sub>-NRs-3 and (f) HRTEM image of CeO<sub>2</sub>-NRs-2 (inset: Fast-Fourier transform pattern image).

ability of holes [43,47]. Meanwhile, the presence of Vo reduces the effective mass of electron because of the relative stronger no-localization of Ce-4f state (Fig. 5b). The smaller the electron effective mass, the higher the mobility of electrons [48]. Therefore, the separation of photo-induced electrons and holes will be enhanced in the oxygen-defective CeO<sub>2</sub>. The Bader charge analysis [49,50] and charge density difference [51,52] (Fig. S2) were also carried out to clarify the effect of oxygen vacancies. As shown in Table S2, the average net charges of surface O atoms on perfect and oxygen-defective CeO<sub>2</sub>(110) are  $-1.143$  and  $-1.178$  lel, and the average net charges of surface Ce are

$+2.302$  and  $+2.246$  lel, respectively. Obviously, more electrons enrich on the surface of oxygen-defective CeO<sub>2</sub>(110) owing to the presence of oxygen vacancies, and therefore an internal electric field is created. As such, the photoexcited electron-hole pairs will be effectively separated, as confirmed by the experimental measurements.

### 3.4. Role of oxygen vacancies on water oxidation

#### 3.4.1. Dehydrogenation of H<sub>2</sub>O

Firstly, the sequential dehydrogenation of water was considered in

**Table 1**

Structure characteristics of pristine and oxygen-defective CeO<sub>2</sub> (<sup>a</sup> obtained from Raman spectra, <sup>b</sup> calculated from XPS analysis).

Samples	Specific surface area/m <sup>2</sup> g <sup>-1</sup>	Length (nm)	Diameter (nm)	Pore size	Pore volume	<sup>a</sup> A <sub>600</sub> /A <sub>450</sub>	<sup>b</sup> Surface Ce <sup>3+</sup> /%
CeO <sub>2</sub> -NRs	98.1	95 $\pm$ 5	9.0 $\pm$ 0.5	16.5	0.180	0.061	12.20
CeO <sub>2</sub> -NRs-1	102.5	80 $\pm$ 5	9.0 $\pm$ 0.5	17.9	0.266	0.202	16.84
CeO <sub>2</sub> -NRs-2	112.5	75 $\pm$ 5	10.0 $\pm$ 0.5	14.6	0.239	0.260	18.75
CeO <sub>2</sub> -NRs-3	94.1	95 $\pm$ 5	10.0 $\pm$ 0.5	19.7	0.244	0.254	17.67

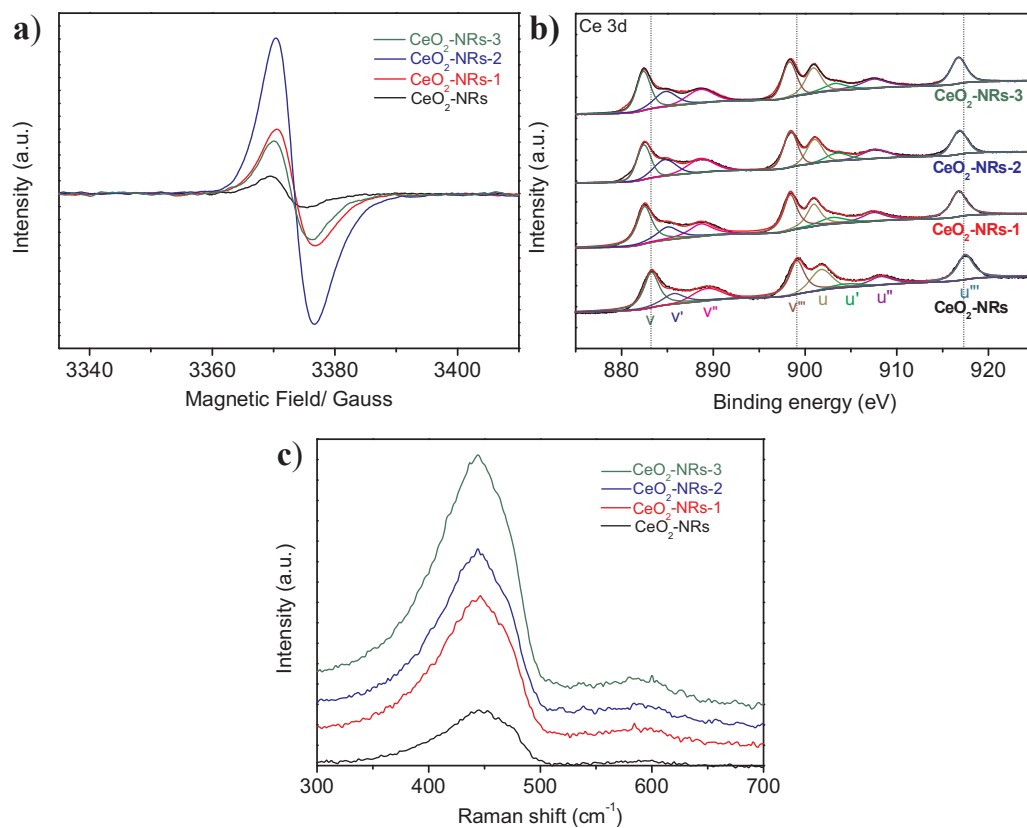


Fig. 3. (a) Room temperature EPR spectra, (b) Ce-3d XPS spectra, and (c) Raman spectra of pristine and oxygen-defective CeO<sub>2</sub>.

the computation, namely  $\text{H}_2\text{O} \rightarrow \text{OH} + \text{H} \rightarrow \text{O} + 2\text{H}$ , as shown in Fig. 6. On perfect CeO<sub>2</sub>(110), H<sub>2</sub>O is adsorbed on the top Ce site with an adsorption energy of  $-76.19 \text{ kJ/mol}$ , close to reported data [53]. The adsorbed H<sub>2</sub>O dehydrogenate to OH and H, and in the final state (FS) OH still binds to the Ce site but H migrates to neighboring top O site.

This step is exothermic by  $-28.93 \text{ kJ/mol}$  with the activation energy of  $7.72 \text{ kJ/mol}$ . Subsequently, the formed OH group dissociates to O and H via the O–H bond scission. This elementary step needs to overcome high activation energy of  $77.15 \text{ kJ/mol}$  with endothermicity of  $67.51 \text{ kJ/mol}$ .

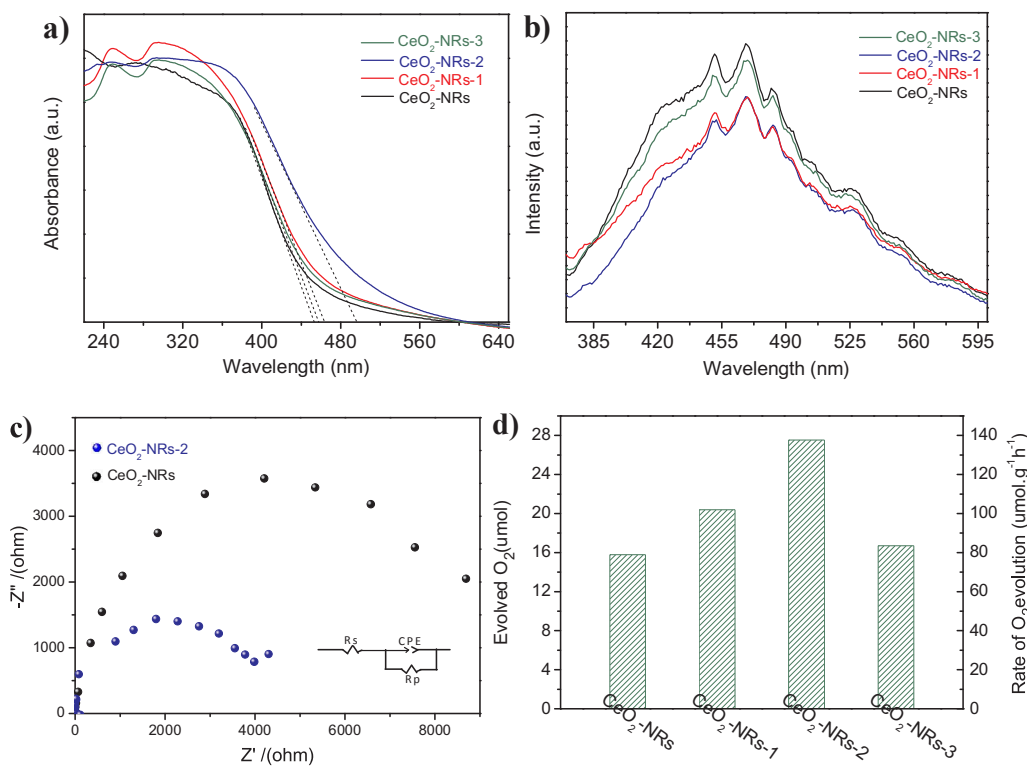
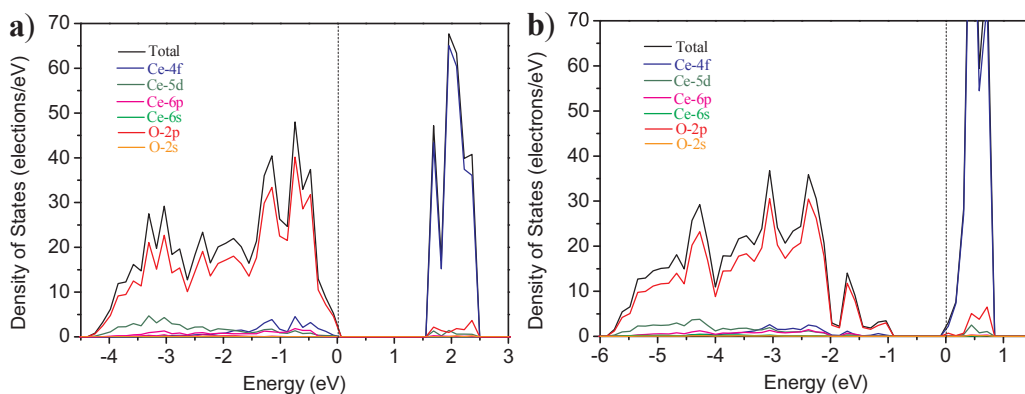


Fig. 4. (a) UV-vis DRS spectra, (b) PL spectra, (c) Electrochemical impedance spectroscopy (EIS), and (d) Visible-light photocatalytic oxygen evolution of pristine and oxygen-defective CeO<sub>2</sub>.



The reaction on oxygen-defective  $\text{CeO}_2(110)$  is similar to the case on perfect  $\text{CeO}_2(110)$ , but easier.  $\text{H}_2\text{O}$  is bounded on Ce site a little weakly ( $-67.51 \text{ kJ/mol}$ ), and undergoes a spontaneous O–H cracking without any activation energy to produce OH and H, with exothermic by  $-71.37 \text{ kJ/mol}$ . Then the OH group further dissociates to H and O with much lower activation energy of  $48.22 \text{ kJ/mol}$  and endothermicity of  $9.64 \text{ kJ/mol}$ , respectively.

It is clear that the dissociation of  $\text{H}_2\text{O}$  to OH and H on  $\text{CeO}_2(110)$  is easy to occur and even barrierless. However, regarding to the further dissociation of OH, there is a fatal problem for perfect  $\text{CeO}_2(110)$ , namely the formed O and H tend to combine with each other to produce OH again, because the reverse  $\text{O} + \text{H} \rightarrow \text{OH}$  reaction is more facile than the forward  $\text{OH} \rightarrow \text{O} + \text{H}$  reaction (activation energy  $9.64 \text{ vs } 77.15 \text{ kJ/mol}$ ). On the oxygen-defective  $\text{CeO}_2(110)$ , fortunately, the OH dehydrogenation is enhanced due to the decreased activation energy ( $48.22 \text{ kJ/mol}$ ), but the reverse recombination reaction is effectively restrained due to the increased binding strength of O + H as a result of more electrons transfer from O to the neighboring Ce (Table S3). Therefore, the presence of oxygen vacancies plays a crucial role in improving the production of O intermediates.

#### 3.4.2. Formation of $\text{O}_2$

Regarding to the O–O bond coupling, two possible ways were considered. For the first one, the second  $\text{H}_2\text{O}$  was dehydrogenated to H and OH, and then the OH combines with the O from the first  $\text{H}_2\text{O}$  molecule to form OOH, namely,  $\text{O} + 2\text{H} + \text{H}_2\text{O} \rightarrow \text{OOH} + 3\text{H}$ . For another one, the second  $\text{H}_2\text{O}$  directly reacts with OH and H of the first  $\text{H}_2\text{O}$  to form HOOH, namely  $\text{OH} + \text{H} + \text{H}_2\text{O} \rightarrow \text{HOOH} + 2\text{H}$ . The corresponding details are presented in the supporting information of Fig. S3, and due to the high activation energy, the HOOH pathway is un-possible on both perfect and oxygen-defective  $\text{CeO}_2(110)$ . Therefore, the first pathway of OOH formation with lower activation energy is considered in the follows.

On the perfect  $\text{CeO}_2(110)$  (Fig. 7, TS4), the O on top Ce site formed

by first  $\text{H}_2\text{O}$  interacts with the OH formed from the dehydrogenation of the second  $\text{H}_2\text{O}$  towards formation of O–O bond in form OOH. This is also verified by the projected density of states (PDOS) analysis (Fig. 8) that shows large overlaps between O-s, p states of O atom from the first  $\text{H}_2\text{O}$  and the s, p states of OH from the second  $\text{H}_2\text{O}$ , suggesting an orbital hybridization occurs for O–O bonding. The formed OOH species bind to Ce site in the FS, which needs to overcome relative high activation energy of  $83.90 \text{ kJ/mol}$  with endothermicity of  $0.96 \text{ kJ/mol}$ . Then the OOH dehydrogenate to  $\text{O}_2$  and H via the O–H bond scission with the activation energy and reaction energy of  $18.32$  and  $-27.00 \text{ kJ/mol}$ , respectively.

On the Oxygen-defective  $\text{CeO}_2(110)$  (Fig. 7, TS6), the distance between O and OH is  $2.394 \text{ \AA}$ , shorter than that on the perfect  $\text{CeO}_2(110)$  ( $2.912 \text{ \AA}$ ), indicating the interaction between O and OH is much stronger on the oxygen-defective surface. This step has a much lower activation energy of  $65.58 \text{ kJ/mol}$  compared with the case of perfect  $\text{CeO}_2(110)$ . Overall the O–O bond formation represents the rate-limiting step in the whole water oxidation, and the presence of oxygen vacancies on  $\text{CeO}_2(110)$  significantly reduces the activation energy of this step, due to the decreased O binding strength with relative less electrons transferred between O and Ce (see Table S4).

The rate constant of key elementary steps involved in water oxidation were calculated according to the harmonic transition theory [54,55]. As shown in Table S5, it is clear that oxygen-defective  $\text{CeO}_2(110)$  has higher rate constant of key elementary steps than that on perfect  $\text{CeO}_2(110)$ . Specially, the rate constant of rate-limiting step on oxygen-defective  $\text{CeO}_2(110)$  is about 2–3 orders of magnitude higher than that on perfect  $\text{CeO}_2(110)$ , confirming the critical roles of oxygen vacancy in water oxidation from the perspective of kinetic.

## 4. Conclusions

We unveiled the important role of oxygen vacancies in photocatalytic water oxidation using  $\text{CeO}_2$  nanorods as model catalyst by

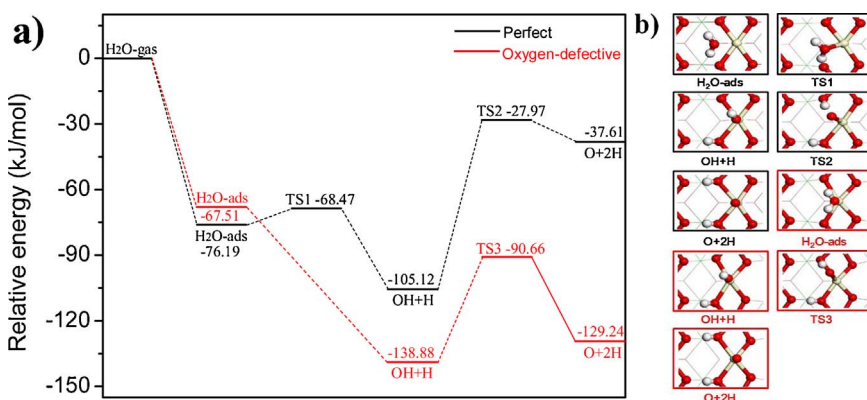
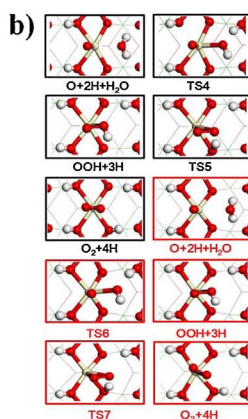
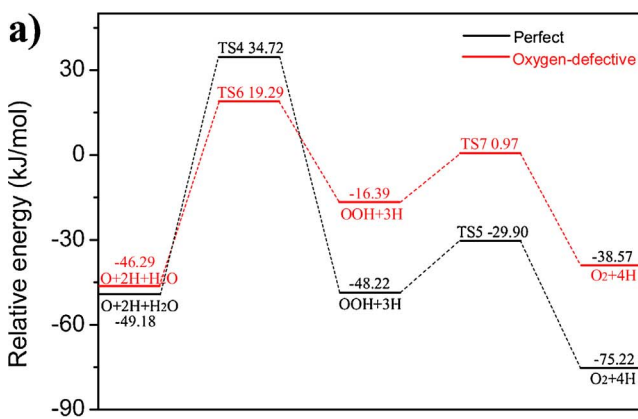
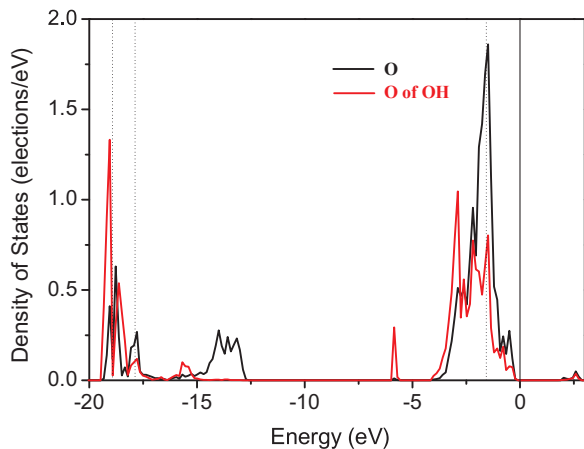


Fig. 6. (a) Potential energy profiles for water dehydrogenation to O, and (b) the corresponding optimized geometries for related states on perfect and oxygen-defective  $\text{CeO}_2(110)$  surfaces.



**Fig. 7.** (a) Potential energy profiles for O–O bond formation, and (b) the corresponding optimized geometries for related states on perfect and oxygen-defective CeO<sub>2</sub>(110) surfaces.



**Fig. 8.** DOS of O (from the first H<sub>2</sub>O) and O (from the second H<sub>2</sub>O) on perfect CeO<sub>2</sub>(110). The solid line at energy zero represents Fermi level, and the dotted lines shows the overlaps between the O and OH.

experimental and DFT studies. CeO<sub>2</sub> nanorods synthesized with in-situ reduction during the hydrothermal growth are abundant with oxygen vacancies from the bulk to surface, with the optical absorption, charge separation and transfer being improved with the increase of oxygen vacancies. The photocatalytic activity also shows good correlation with the concentration of oxygen vacancies. Furthermore, DFT + U calculation shows the presence of oxygen vacancies on CeO<sub>2</sub>(110) effectively narrows the band gap and accelerates the charge separation by regulating the electronic structure. More importantly, on oxygen-defective CeO<sub>2</sub>(110) the barrier energy for the rate limiting step of O–O bond formation in the whole water oxidation is decreased, along with restraining the reverse reaction of O and H, thus the O<sub>2</sub> generation kinetics are improved significantly.

### Competing interest

The authors declare no competing financial interest.

### Acknowledgment

The authors appreciate the support from the National Natural Science Foundation of China (51661145026, 21676193, 21506156), the Tianjin Municipal Natural Science Foundation (15JCZDJC37300, 16JCQNJC05200) and Pakistan Science Foundation PSF/257NSFC-Eng/P-UOL(02).

### Appendix A. Supplementary data

Supplementary data associated with this article can be found, in the online version, at <http://dx.doi.org/10.1016/j.apcatb.2017.10.049>.

### References

- [1] J. Luo, J.-H. Im, M.T. Mayer, M. Schreier, M.K. Nazeeruddin, N.-G. Park, S.D. Tilley, H.J. Fan, M. Grätzel, *Science* 345 (2014) 1593–1596.
- [2] J. Liu, Y. Liu, N. Liu, Y. Han, X. Zhang, H. Huang, Y. Lifshitz, S.-T. Lee, J. Zhong, Z. Kang, *Science* 347 (2015) 970–974.
- [3] S.J. Moniz, S.A. Shevlin, D.J. Martin, Z.-X. Guo, J. Tang, *Energy Environ. Sci.* 8 (2015) 731–759.
- [4] B. Qiu, Q. Zhu, M. Du, L. Fan, M. Xing, J. Zhang, *Angew. Chem. Int. Ed.* 129 (2017) 2728–2732.
- [5] M. Xing, B. Qiu, M. Du, Q. Zhu, L. Wang, J. Zhang, *Adv. Funct. Mater.* 27 (2017) 1702624–1702633.
- [6] D.J. Martin, K. Qiu, S.A. Shevlin, A.D. Handoko, X. Chen, Z. Guo, J. Tang, *Angew. Chem. Int. Ed.* 53 (2014) 9240–9245.
- [7] J. Ryu, S.H. Lee, D.H. Nam, C.B. Park, *Adv. Mater.* 23 (2011) 1883–1888.
- [8] Q. Yin, J.M. Tan, C. Besson, Y.V. Geletii, D.G. Musaev, A.E. Kuznetsov, Z. Luo, K.I. Hardcastle, C.L. Hill, *Science* 328 (2010) 342–345.
- [9] M. Tahir, L. Pan, F. Idrees, X. Zhang, L. Wang, J.-J. Zou, Z.L. Wang, *Nano Energy* 37 (2017) 136–157.
- [10] F. Iyu, Y. Bai, Z. Li, W. Xu, Q. Wang, J. Mao, L. Wang, X. Zhang, Y. Yin, *Adv. Funct. Mater.* 27 (2017) 1702324–1702331.
- [11] T. Montini, M. Melchionna, M. Monai, P. Fornasiero, *Chem. Rev.* 116 (2016) 5987–6041.
- [12] A. Primo, T. Marino, A. Corma, R. Molinari, H. Garcia, *J. Am. Chem. Soc.* 133 (2011) 6930–6933.
- [13] H.Z. Zhu, Y.M. Lu, F.J. Fan, S.H. Yu, *Nanoscale* 5 (2013) 7219–7223.
- [14] W. Lei, T. Zhang, L. Gu, P. Liu, J.A. Rodriguez, G. Liu, M. Liu, *ACS Catal.* 5 (2015) 4385–4393.
- [15] D. Jiang, W. Wang, L. Zhang, Y. Zheng, Z. Wang, *ACS Catal.* 5 (2015) 4851–4858.
- [16] X. Liu, K. Zhou, L. Wang, B. Wang, Y. Li, *J. Am. Chem. Soc.* 131 (2009) 3140–3141.
- [17] G. Wang, Y. Ling, Y. Li, *Nanoscale* 4 (2012) 6682–6691.
- [18] F. Lei, Y. Sun, K. Liu, S. Gao, L. Liang, B. Pan, Y. Xie, *J. Am. Chem. Soc.* 136 (2014) 6826–6829.
- [19] G. Wang, H. Wang, Y. Ling, Y. Tang, X. Yang, R.C. Fitzmorris, C. Wang, J.Z. Zhang, Y. Li, *Nano Lett.* 11 (2011) 3026–3033.
- [20] Z.-F. Huang, J. Song, L. Pan, X. Jia, Z. Li, J.-J. Zou, X. Zhang, L. Wang, *Nanoscale* 6 (2014) 8865–8872.
- [21] Z.-F. Huang, J. Song, L. Pan, F. Lv, Q. Wang, J.-J. Zou, X. Zhang, L. Wang, *Chem. Commun.* 50 (2014) 10959–10962.
- [22] J. Song, Z.-F. Huang, L. Pan, J.-J. Zou, X. Zhang, L. Wang, *ACS Catal.* 5 (2015) 6594–6599.
- [23] M.M. Khan, S.A. Ansari, D. Pradhan, D.H. Han, J. Lee, M.H. Cho, *Ind. Eng. Chem. Res.* 53 (2014) 9754–9763.
- [24] I. Funes-Ardoiz, P. Garrido-Barros, A. Llobet, F. Maseras, *ACS Catal.* 7 (2017) 1712–1719.
- [25] S. Lin, X. Ye, X. Gao, J. Huang, *J. Mater. Chem. A Chem.* 406 (2015) 137–144.
- [26] Y. Ping, R.J. Nielsen, W.A. Goddard III, *J. Am. Chem. Soc.* 139 (2016) 149–155.
- [27] W. Gao, Z. Zhang, J. Li, Y. Ma, Y. Qu, *Nanoscale* 7 (2015) 11686–11691.
- [28] G. Kresse, J. Hafner, *Phys. Rev. B* 48 (1993) 13115–13118.
- [29] G. Kresse, J. Furthmüller, *Phys. Rev. B Condens. Matter Mater.* 54 (1996) 11169–11186.
- [30] J.P. Perdew, Y. Wang, *Phys. Rev. B Condens. Matter Mater.* 45 (1992) 13244–13249.
- [31] S. Dudarev, G. Botton, S. Savrasov, C. Humphreys, A. Sutton, *Phys. Rev. B* 57 (1998) 1505–1509.

[32] Z. Yang, X. Yu, Z. Lu, S. Li, K. Hermansson, *Phys. Lett. A* 373 (2009) 2786–2792.

[33] D. Sheppard, P. Xiao, W. Chemelewski, D.D. Johnson, G. Henkelman, *J. Chem. Phys.* 136 (2012) 0741031–0741038.

[34] E. Kümmel, G. Heger, *J. Solid State Chem.* 147 (1999) 485–500.

[35] H.Y. Li, H.F. Wang, Y.L. Guo, G.Z. Lu, P. Hu, *Chem. Commun.* 47 (2011) 6105–6107.

[36] M.V. Ganduglia-Pirovano, J.L. Da Silva, J. Sauer, *Phys. Rev. Lett.* 102 (2009) 0261011–0261014.

[37] N. Zhang, X. Li, H. Ye, S. Chen, H. Ju, D. Liu, Y. Lin, W. Ye, C. Wang, Q. Xu, J. Zhu, L. Song, J. Jiang, Y. Xiong, *J. Am. Chem. Soc.* 138 (2016) 8928–8935.

[38] M. Guo, J. Lu, Y. Wu, Y. Wang, M. Luo, *Langmuir* 27 (2011) 3872–3877.

[39] A.A. Vernekar, T. Das, G. Muges, *Angew. Chem. Int. Ed.* 128 (2016) 1434–1438.

[40] L. Pan, S. Wang, J. Xie, L. Wang, X. Zhang, J.-J. Zou, *Nano Energy* 28 (2016) 296–303.

[41] X. Jia, M. Tahir, L. Pan, Z.-F. Huang, X. Zhang, L. Wang, J.-J. Zou, *Appl. Catal. B Environ.* 198 (2016) 154–161.

[42] L. Pan, T. Muhammad, L. Ma, Z.-F. Huang, S. Wang, L. Wang, J.-J. Zou, X. Zhang, *Appl. Catal. B Environ.* 189 (2016) 181–191.

[43] L. Pan, S. Wang, W. Mi, J. Song, J.-J. Zou, L. Wang, X. Zhang, *Nano Energy* 9 (2014) 71–79.

[44] Y. Huang, C.-F. Yan, C.-Q. Guo, Y. Shi, *Int. J. Hydrogen Energy* 41 (2016) 7919–7926.

[45] J.P. Perdew, M. Levy, *Phys. Rev. Lett.* 51 (1983) 1884–1887.

[46] J. Liu, J. Song, H. Niu, L. Pan, X. Zhang, L. Wang, J.-J. Zou, *Appl. Surf. Sci.* 371 (2016) 61–66.

[47] G. Liu, P. Niu, C. Sun, S.C. Smith, Z. Chen, G.Q. Lu, H.M. Cheng, *J. Am. Chem. Soc.* 132 (2010) 11642–11648.

[48] J. Qiao, X. Kong, Z.X. Hu, F. Yang, W. Ji, *Nat. Commun.* 5 (2014) 4475–4481.

[49] G. Henkelman, A. Arnaldsson, H. Jónsson, *Comput. Mater. Sci.* 36 (2006) 354–360.

[50] Y.-C. Zhang, L. Pan, J. Lu, J. Song, Z. Li, X. Zhang, L. Wang, J.-J. Zou, *Appl. Surf. Sci.* 401 (2017) 241–247.

[51] J. Li, W. Cui, Y. Sun, Y. Chu, W. Cen, F. Dong, *J. Mater. Chem. A* 5 (2017) 9358–9364.

[52] T. Xiong, W. Cen, Y. Zhang, F. Dong, *ACS Catal.* 6 (2016) 2462–2472.

[53] M. Molinari, S.C. Parker, D.C. Sayle, M.S. Islam, *J. Phys. Chem. C* 116 (2012) 7073–7082.

[54] J.P. Clay, J.P. Greeley, F.H. Ribeiro, W. Nicholas Delgass, W.F. Schneider, *J. Catal.* 320 (2014) 106–117.

[55] G. Li, J. Han, H. Wang, X. Zhu, Q. Ge, *ACS Catal.* 5 (2015) 2009–2016.